Journal of Power Sources 237 (2013) 33–40

Contents lists available at SciVerse ScienceDirect

Journal of Power Sources

journal homepage: www.elsevier.com/locate/jpowsour

# In situ formation of a solid oxide fuel cell (SOFC) cermet anode by $NiWO_4$ reduction

Edward M. Sabolsky [a,*], Phil Gansor [a], Engin Çiftyürek [a], Katarzyna Sabolsky [a], Chunchuan Xu [b], John W. Zondlo [b]

[a] Department of Mechanical and Aerospace Engineering, West Virginia University, PO Box 6106, Morgantown, WV 26506, USA
[b] Department of Chemical Engineering, West Virginia University, PO Box 6106, Morgantown, WV 26506, USA

## HIGHLIGHTS

- SOFC cermet anode *in situ* synthesized by reduction of $NiWO_4$ composition.
- XPS analysis showed that anode was composed of Ni, W, $WO_2$, and $WO_3$ mixture.
- Electrolyte-supported SOFC showed 104 mW $cm^{-2}$ (800 °C) with unoptimized microstructure.
- Gd-doped ceria additions to $NiWO_4$ anode increased SOFC performance.

## ARTICLE INFO

*Article history:*
Received 10 September 2012
Received in revised form
27 February 2013
Accepted 1 March 2013
Available online 14 March 2013

*Keywords:*
SOFC
Anode
Cermet
*In situ* reduction
$NiWO_4$
Phosphine

## ABSTRACT

The presented work describes a process for producing a mixed-conducting SOFC cermet anode through the *in situ* reduction of a ternary oxide. A porous nickel tungstenate ($NiWO_4$) was screen-printed and bonded onto an yttrium-stabilized zirconia (YSZ) electrolyte-supported SOFC by treatment at 1000 °C for 1 h. An (La,Sr)$MnO_3$/$Ce_{0.9}Gd_{0.1}O_2$(LSM/GDC) was utilized as the cathode with the NiWO4 acting as the anode for the SOFC. The ~1-cm diameter fuel cell with a ~100-μm thick YSZ electrolyte was tested in $H_2$ fuel at 800 °C. During the insertion of the $H_2$ fuel, the $NiWO_4$ was reduced to form a Ni/$WO_x$ cermet composite that consisted of a fine mixture of Ni-nanoparticles dispersed over the porous $WO_x$ support structure. A maximum power density of ~104 mW $cm^{-2}$ was attained for the reduced $NiWO_4$ anode, even with an un-optimized and dense microstructure, on an electrolyte-supported cell. The power density was increased to ~165 mW $cm^{-2}$ with the incorporation of GDC powder into the $NiWO_4$ anode. The same $NiWO_4$/GDC composite was tested within a fuel stream of $H_2$ containing 10 ppm $PH_3$. The cell's degradation rate was 0.006 V $h^{-1}$ for 5 h at 750 °C, which is similar to that observed for conventional Ni/YSZ cermets.



## 1. Introduction

The traditional anode composition for solid oxide fuel cell (SOFC) applications is a Ni-cermet, typically consisting of a porous composite of Ni metal and yttrium-stabilized zirconia (YSZ) or doped-ceria ($CeO_2$). This cermet is processed by creating a composite mixture of NiO and electrolyte oxide powders. After incorporation into the SOFC architecture by conventional ceramic processing methods (such as tape-casting or screen-printing), the Ni-cermet composition is formed during fuel cell operation when the oxide composite is reduced by the reducing fuel [1,2]. Although SOFCs using Ni-cermet anodes continue to show excellent electrochemical performance, alternative anode materials are still attractive to reduce cost and increase applicability to other fuel streams. With respect to applicability, the Ni within SOFC anodes is known to coke with hydrocarbon or coal-derived fuels (coking) and/or to react with impurities that form resistive secondary phases (fouling). Fouling and coking of the Ni-cermet anode results in a combination of decreased thermomechanical stability, electrochemical activity, and mass transport [3–6]. For these reasons, the partial (or full replacement) of Ni within SOFC anodes has been the focus of many researchers over the past few decades [4–13].

* Corresponding author. Tel.: +1 304 293 3272; fax: +1 304 293 6689.
*E-mail addresses:* Ed.sabolsky@mail.wvu.edu (E.M. Sabolsky), pgansor@mix.wvu.edu (P. Gansor), eciftyur@mix.wvu.edu (E. Çiftyürek), Kathy.sabolsky@mail.wvu.edu (K. Sabolsky), Chunchuan.Xu@mail.wvu.edu (C. Xu), John.zondlo@mail.wvu.edu (J.W. Zondlo).

0378-7753/$ – see front matter © 2013 Elsevier B.V. All rights reserved.
http://dx.doi.org/10.1016/j.jpowsour.2013.03.011

The alternative anode compositions that were primarily centered upon by researchers were Cu-based cermets or oxide-based compositions [4–13]. Ceramic-based compositions such as doped-$SrTiO_3$, $La_{0.75}Sr_{0.25}Cr_{0.5}Mn_{0.5}O_3$ (LSCM) and $Sr_2MgMoO_{6-\delta}$ (SMM) have shown adequate mechanical stability, electrical conductivity, coking stability, ionic conduction and fuel oxidation kinetics when combined with other metal catalysts. In a few cases, these compositions were used to fabricate an all-ceramic, anode-supported structure in order to improve power performance, yet the ceramic support structure still required the incorporation of nickel or copper for enhanced performance [7–9].

A few researchers tested SOFCs containing tungsten (W) as a replacement for Ni within the anode structure with varying results [14–17]. In other related electrochemical applications, researchers have also demonstrated that various Ni–W composite oxide compositions could be used as a dehydrogenation catalyst [17], polymer fuel cell electrodes [19], $H_2S$ sensing materials [20,21], and hydrodesulfurization (HDS) catalysts [22]. Recently, Torabi et al. showed some promising results using a tungsten carbide (WC)-based anode for SOFCs functioning on hydrogen and/or methane as the fuel [16,17]. The use of hydrogen fuel resulted in reduction of the 25 vol% WC/75 vol% YSZ anode at OCV, but insertion of methane stabilized the carbide phase at 800 °C. The anode polarization was shown to be 7.7 Ω $cm^2$ at 800 °C in 80% $H_2$–20% $CH_4$ fuel from symmetrical cell tests [16]. This anode polarization was decreased to 1.45 Ω $cm^2$ with the addition of Ni and $CeO_2$ to the WC/YSZ anode [17]. A maximum power density of ~100 mW $cm^2$ (850 °C) in the stated fuel was obtained for this Ni–$CeO_2$–WC–YSZ anode printed onto an electrolyte-supported cell (ohmic resistance ~0.4 Ω $cm^2$) with a LSM/YSZ cathode. Hussain et al. also recently presented a preliminary study of a $WO_3$-infiltrated 0.48W–0.52Cu–ScYSZ (WCS) anode for intermediate SOFC applications [23]. Hussain et al. measured an electrode polarization of ~11 Ω $cm^2$ at 600 °C by electrochemical impedance spectroscopy (EIS) for this composition in $H_2$ using a symmetrical cell configuration. The state of the $WO_3$ during and after testing was not characterized in the work, and the anode composition was never tested on a full SOFC platform. Therefore, a $WO_3$-based anode composition, as the main constituent or within a cermet composition, for SOFC applications has not been reported in literature.

An interesting candidate for an SOFC anode is the $NiWO_4$ composition. The $NiWO_4$ composition has a general wolframite structure that can be readily reduced to Ni–$WO_{3-x}$ mixtures at various oxygen partial pressures [24–26]. The defective $WO_3$ composition is a known mixed ion-electron conductor (MIEC), which can potentially substitute for the use of doped-$ZrO_2$ and $CeO_2$ typically used within the SOFC anode [27–30]. At high $H_2$ content and low oxygen partial pressures, the $NiWO_4$ composition reduces to a mixture of Ni metal and $WO_x$; with further decreases in the oxygen partial pressure, the $WO_3$ can reduce to $WO_2$ and finally to elemental W [24–26]. Therefore, depending upon the $H_2$ fuel concentration and current load, the anode may consist of a mixture of nano-Ni supported upon a mixture of $WO_3$/$WO_2$/W. This redox characteristic provides an opportunity to form *in situ* a Ni cermet directly from the ternary oxide composition.

Catalyst researchers have shown methods of *in situ* reduction of complex ternary oxide solid-solutions to form oxide-supported nano-metal catalysts for various reforming applications [31–33]. This process is dependent upon forming an oxide compound with base and/or precious metals dissolved into one of the crystal structure sites. With the application of a reducing gas stream, the most unstable metal oxide dopants may be reduced at the surface of these particles. The process may continue as the developing concentration gradients force further migration of the dopant to the surface. For example, Goldwasser et al. formed a perovskite solid solution of $La_{1-x}Ca_xRu_{0.8}Ni_{0.2}O_3$ [32,33]. During the methane reforming application, a homogenous mixture of 9–17 nm Ni catalyst particles precipitated over the lanthanum ruthenate support particles to enhance catalytic activity. Another example is the α- and β-phase $NiMoO_4$ catalyst composition used as an oxidative dehydrogenation catalyst for various light paraffins [34–37]. Depending upon the reactant gas, oxygen partial pressure and temperature, the catalyst can be reduced to a cermet composition consisting of nano-Ni metal particles dispersed over $MoO_x$ particles. Therefore, the *in situ* reduction the $NiWO_4$ composition should produce a similar cermet microstructure under the SOFC testing conditions. The objectives of the present work were two-fold. The first objective was to evaluate the viability of *in situ* reducing the $NiWO_4$ composition to form a Ni/$WO_x$ cermet for application as a potential SOFC anode. Fuel cell tests (current–voltage–power measurements) were used to measure the electrochemical performance of the initial trial of this anode composition. The incorporation of finite amounts of YSZ and Gd-doped $CeO_2$ (GDC) electrolytes within the $NiWO_4$ composition were also investigated in order to assess effects on the thermo-mechanical stability and electrochemical performance. Detailed XPS analysis was carried out to determine the chemical state of the dissociated $WO_x$ and Ni at different locations throughout the anode. This characterization is important to better understand the contribution of each component to the anode electrical and electrochemical activity.

The second objective was to evaluate quickly the stability of the same Ni/$WO_x$ cermet anode mixture within a $H_2$ fuel stream containing $PH_3$ impurities. The typical Ni/YSZ anode exhibits difficulty in stable functioning on fuel streams loaded with contaminants such as S, P, Sb, Cl, Zn, As, and HCl that react with the Ni-based anodes and quickly degrade the performance of the SOFC at standard operating temperatures [3,38]. Among the most reactive with nickel is phosphorus, and currently there are no SOFC anode compositions stable in the presence of phosphine. It has been reported that the loss in cell performance originates from zirconia phosphate (and potentially metastable phosphides during high-temperature testing) formation at the anode/electrolyte active interface [12,39–42]. Due to previous demonstrations of stable and increased catalyst performance of the Ni–W composite catalyst in the presence of phosphorus [18,23], the electrochemical stability of the $NiWO_4$-derived anode was tested as a function of time in $H_2$ fuel with 10 ppm $PH_3$ impurity. The fuel cell tests in $PH_3$-containing $H_2$ fuel will provide insight for potential operation with contaminated coal syngas fuel streams.

## 2. Experimental

Although the overall performance of the fuel cell is known to be low, an electrolyte-supported SOFC architecture was utilized in order to provide a simple platform to alter the anode composition without requiring alterations to the electrolyte and cathode microstructures. The active anode layer is considered to be the first ~15–20 μm layer (of one specific composition and microstructure) in contact with the electrolyte. The active anodes tested in this work were: 1) pure $Ce_{0.9}Gd_{0.1}O_2$ (GDC), 2) standard Ni/YSZ cermet, 3) pure $NiWO_4$, 4) $NiWO_4$/YSZ composite, and 5) $NiWO_4$/GDC composite. A $NiWO_4$ current collection layer was printed over all active layers accept the pure GDC layer. Commercial $NiWO_4$ powder (Alfa Aesar, USA) with an average particle size of ~5 μm was used within the anode experiments.

The electrolyte-support membranes were fabricated from 8 mol % YSZ powder (Daiichi Kigenso Kagaku Kogoyo Co., LTD, Japan) by a tape-casting and lamination process. The 1-cm diameter YSZ button cell membranes were sintered at 1450 °C for 2 h to full density. A ~3-μm thick $Ce_{0.9}Gd_{0.1}O_2$ (GDC) buffer layer was incorporated

between the electrolyte and electrodes by screen-printing for both the anode and cathode in an effort to prevent possible interfacial reactions with the $ZrO_2$. The GDC was synthesized using a co-precipitation and calcination method. This material was then screen-printed and fired onto the electrolyte at 1350 °C. Each of the subsequent anode compositions was sintered at the minimum temperature necessary for adhesion to the electrolyte. A standardized $La_{0.85}Sr_{0.15}MnO_3$ (LSM) based cathode was used for each test to keep the anode composition as the primary variable. The cathode consisted of a 10 μm LSM/GDC active cathode layer which was printed and dried before adding a 40 μm LSM current collector layer. The cathode assembly was sintered at 1100 °C for 1 h.

The current collection contact layer for the $NiWO_4$ containing anodes was comprised of the original $NiWO_4$ composition painted thinly over a Pt mesh. For the GDC anode, a thin layer of GDC was used to bond the Pt mesh to the outer surface of the cell. A thin layer of Ni metal paint was used for the Ni/YSZ cermet anode to bond the mesh in place. Upon sealing of the system with mica rings and sufficient compression, the cell was heated to 800 °C over 4 h with 50 sccm $N_2$ flow on the anode and 50 sccm air on the cathode. Once the operating temperature was achieved, the anode stream was slowly altered over 2 h by incrementally increasing the flow of $H_2$. Wet $H_2$ at a flow rate of 100 sccm was used as the anode testing condition (97% $H_2$, 3% $H_2O$) with 100 sccm air for the cathode. Cell polarization curves (*I–V* curves) and electrochemical impedance spectra were taken during the test to establish baseline cell performance. These data were collected using a solid-state load cell for constant DC load (TDI Transistor Device SD-1103) and a Solartron SI-1287 interface and an SI-1252 frequency response analyzer for the electrochemical impedance spectroscopy (EIS).

In order to obtain the chemical states and a composition profile of the nickel (Ni) and tungsten (W) throughout the SOFC anode, X-Ray Photoelectron Spectroscopy (XPS, PHI 5000 Versaprobe) was utilized. The SOFC studied in this work utilized a pure $NiWO_4$ anode on the electrolyte-supported cell platform previously described. The cell was held under constant current load (0.1 A $cm^{-2}$) at 800 °C for 12 h, and then the sample was cooled quickly in $H_2$ to room temperature. XPS spectra were analyzed by PHI SUMMIT software. The X-ray source was operated at 15 kV and 25 W using Al Kα (1486.6 eV) radiation. Prior to spectral analysis, the surface of the cell was cleaned to remove atmospheric and post-test contaminations with $Ar^+$ sputtering by means of a 2 kV accelerating voltage for 30 s. Depth profile analysis was conducted with $Ar^+$ stepwise sputtering using an accelerating voltage of 4 kV and an etching area of 1 × 1 mm. The X-ray data acquisition area was 100 μm × 100 μm. All binding energies of W, O and Ni were referenced to Au $4_{f7/2}$ at 84.0 eV.

## 3. Results and discussion

### 3.1. Voltage–current–power testing of $NiWO_4$ anode

As previously stated, the $NiWO_4$ was deposited by screen-printing onto an electrolyte-support consisting of a ~120 μm thick YSZ-supported membrane with a thin, dense GDC coating. The porous $NiWO_4$ was bonded onto the membrane at a temperature of 1000 °C for 1 h, which is ~300 °C lower in temperature than typical NiO/YSZ mixtures. This adhesion temperature is close to that utilized for typical lanthanum ferrite and cobaltite cathode compositions, potentially allowing for co-firing of both the anode and cathode compositions for specific SOFC architectures. After full reduction of the anode in the 3% wet $H_2$, the anode remained firmly attached to the electrolyte membrane.

The voltage–current–power (*V–I–P*) measurement was completed on the fuel cell down to a current density of ~0.3 A $cm^{-2}$ at 800 °C. All fuel cells were tested with the same protocol previously described, and after reduction, all cells showed a similar OCV value of ~1.06–1.07 V. In order to define a baseline for the fuel cell architecture, a traditional Ni/YSZ anode was tested on the electrolyte-supported platform using the same cathode (LSM/GDC) and electrolyte (YSZ) previously described. The standard Ni/YSZ cermet was fabricated by screen-printing a ~15 μm thick NiO/YSZ active layer (50/50 wt%) and ~35 μm thick NiO/YSZ current collector layer (70/30 wt%). Following the same reduction processes discussed in the Experimental section above, the cermet was formed during the 2 h reduction process before loading. Fig. 1 (data set *a*) shows the *V–I–P* data for this baseline sample, which demonstrated an ASR of ~1.06 Ω $cm^{-2}$. The area specific resistance (ASR) for the cell was calculated from the fitted slope of the voltage versus current density data. The maximum power density for this SOFC was ~254 mW $cm^{-2}$ (at 0.51 A $cm^{-2}$). Fig. 1 (data set *b*) shows the *V–I–P* data collected for one of the electrolyte-supported SOFCs with the reduced $NiWO_4$ anode. From this current sweep, a maximum power density of ~104 mW $cm^{-2}$ (at 0.26 A $cm^{-2}$) was attained. The ASR value for the loading sweep was ~2.51 Ω $cm^{-2}$. Subsequent tests with the pure $NiWO_4$ anode composition (and microstructure) yielded similar performance, which is ~40% the performance demonstrated by the SOFC with the standard Ni/YSZ anode. Although this anode performance was lower than the baseline Ni/YSZ cermet, the power achieved from this cell shows the potential for *in situ* forming a functioning cermet anode from a singular ternary oxide composition.

In order to further compare against the Ni/YSZ cermet, the electrolyte phase (YSZ) was included with the $NiWO_4$ composition to form a 50/50 vol% $NiWO_4$/YSZ mixture within the active layer. The pure $NiWO_4$ composition was used as the current collection layer and was retained throughout all the $NiWO_4$ experiments. Fig. 1 (data set *c*) displays the *V–I–P* data collected for the testing of this composite anode. The $NiWO_4$/YSZ mixture showed a slight increase in performance with an ASR ≈1.93 Ω $cm^{-2}$, with a maximum power density of 116 mW $cm^{-2}$ (at 0.31 A $cm^{-2}$) with this modification. One possible explanation for this slight performance increase is due to the increase in overall ionic conduction of the composite (due to the incorporation of the electrolyte material in the anode). It is assumed at this point that the $NiWO_4$ composition is reducing to a Ni–W metallic mixture during testing, and the ionic contribution is quite limited (due to the low availability of $WO_{3-x}$ within the resultant reduce composition). The

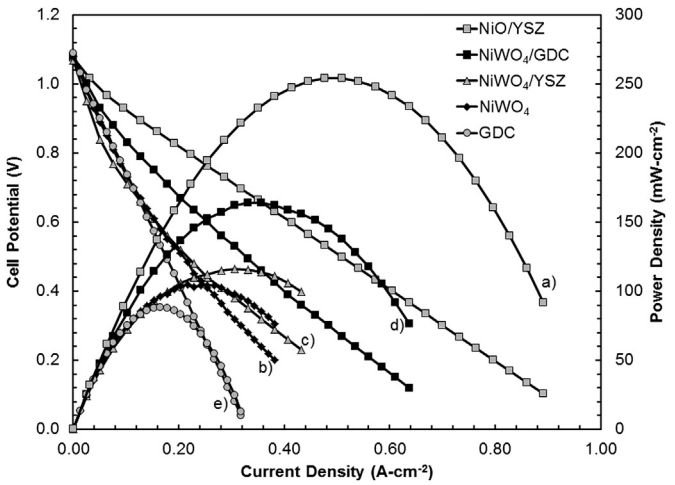


**Fig. 1.** Cell potential–power density–current density performance for an electrolyte-supported SOFC button cell at 800 °C. The data sets for the following anode compositions are included: a) NiO/YSZ, b) $NiWO_4$, c) $NiWO_4$/YSZ, d) $NiWO_4$/GDC, and e) GDC.

characterization of the phase state during testing will be discussed in the subsections below. In order to demonstrate the electronic contribution of the $NiWO_4$ composition, the $NiWO_4$ ink was printed and fired (using the same conditions stated above) to a thickness of ~30 μm over four platinum thin film leads on an YSZ substrate. Four-point conductivity measurements of the porous film were completed at 800 °C in air and $H_2$ reducing conditions. In air, the sample showed a conductivity of ~1 S $cm^{-1}$, but after reduction, the same film showed a conductivity of ~640 S $cm^{-1}$. This result indicates the high electronic character of the reduced composition and the potential need for a high ionic contribution level. The increased power density may also be attributed to a general modification in the microstructure that would affect anything from the charge transfer to the fuel/steam transport. For the $NiWO_4$/YSZ composite, a higher adhesion temperature (1150 °C) was required to bond the active layer to the GDC barrier layer. This increased temperature led to further densification of the anode which would limit diffusion and could explain the limited increase in performance.

In an effort to reduce the sintering temperature needed for sufficient adhesion, the YSZ was replaced in the active anode layer with GDC. The resultant 50/50 vol% $NiWO_4$/GDC mixture anode sintered onto the electrolyte at 1050 °C. This composite anode displayed an ASR of 1.57 Ω $cm^{-2}$ over the linear (ohmic limited) portion of the *V–I* data and generated a maximum power density of ~164 mW $cm^{-2}$ (at 0.36 A $cm^{-2}$) at 800 °C using wet $H_2$ fuel (Fig. 1, data set *d*). To better understand the contribution of the GDC, a similar fuel cell consisting of only a porous GDC anode (with no $NiWO_4$ component) was tested at the same conditions. The GDC layer was fired onto the GDC-coated YSZ membrane (of the same thickness) at 1100 °C for 1 h Fig. 1 (data set *e*) shows the *V–I–P* data collected from testing this cell at the same conditions previously used for the other anode architectures. The cell showed an ASR of 3.24 Ω $cm^{-2}$ at 800 °C in $H_2$ and a maximum power density of ~82 mW $cm^{-2}$ (at 0.17 A $cm^{-2}$). The pure GDC anode demonstrated ~70% of the performance of the reduced $NiWO_4$ composition, and nearly 50% of the $NiWO_4$/GDC anode mixture.

From the comparison of the maximum power densities and average ASR values calculated at the higher current loads (>0.2 A $cm^{-2}$) for each anode composition, it appears that the reduced $NiWO_4$ anode significantly lacks the contribution of an ionic carrier phase and that the present W-oxide phases are not sufficient for oxygen transport and/or exchange. Only when an electrolyte phase, such as GDC or YSZ, is incorporated within the resultant Ni–$WO_x$ cermet, can the cell be driven to the higher powers at these higher current densities. Interestingly, the analysis of the lower current density loads (or lower drive voltages) presents a different trend. At a constant voltage of 0.7 V, the current densities for the Ni/YSZ, $NiWO_4$, $NiWO_4$/YSZ, $NiWO_4$/GDC, and GDC anodes were 0.31, 0.12, 0.11, 0.19, and 0.11 A $cm^{-2}$, respectively. This resulted in a similar average power density of ~76–80 mW $cm^{-2}$ for the $NiWO_4$, $NiWO_4$/YSZ, and GDC anodes. From this data, it appears that at lower loads, these three anodes perform quite similarly. The Ni/YSZ and $NiWO_4$/GDC anode displayed greater than a 2.5 and 1.7 times increase in performance over these three anodes, respectively. Therefore, the combined minimum level of electronic conduction, hydrogen adsorption, ionic transport, and charge-transfer capacity of the Ni/$WO_x$ anode (reduced $NiWO_4$) is similar to that of the porous GDC anode used in this work. Of course the limiting mechanism for the hydrogen oxidation rate for the reduced $NiWO_4$ and GDC anodes would be different; it may be assumed again that the Ni/$WO_x$ would not be limited by hydrogen adsorption (due to the high volume of Ni metal) or electronic conduction (as discussed above), but these may limit the performance of the pure GDC anode. Thus, as the current is driven to higher levels (>0.2 A $cm^{-2}$), the ionic contribution of the Ni/$WO_x$ anodes appears not to be sufficient to support the minimum oxygen transport and charge-transfer required for increased oxidation kinetics. The addition of the GDC electrolyte phase to the $NiWO_4$ material was shown to assist in these deficiencies (both at low and high currents), and the higher electrochemical performance was realized. The incorporation of the YSZ electrolyte phase into the $NiWO_4$ anode should have resulted in a similar increase in the lower current performance, but this was not the case in this work. The reason is still not clear for this discrepancy in the performance trend and relation, and further work will need to be completed to define this difference, as well as the relative contributions of the electrolyte additives to the anode polarization resistance (and thus, anode reaction mechanisms).

Figs. 2 and 3 display the back-scattered SEM micrographs of the anode structure before reduction and after testing in $H_2$ for 48 h, respectively. The samples were mounted in epoxy and polished down to 1800 grit diamond. Fig. 2 shows that the virgin anode consists of a singular phase with evenly-dispersed porosity throughout the microstructure. The grain size of the $NiWO_4$ grains ranges between 0.5 and 3.0 μm. The porosity level was measured by image analysis (NIH ImageJ), and an average porosity of ~30% was seen before reduction. Fig. 3 shows the back-scattered SEM micrograph of the same microstructure after testing in $H_2$ fuel for 48 h. This micrograph shows the opposite of what was expected, in that the level of porosity actually decreased. The micrograph displays a dense microstructure with the occasional elongated coarse pores, and the differentiation of the Ni, W and/or $WO_x$ grains are difficult to distinguish from the SEM micrographs. Additionally, there was a significant change to the particle geometry, where the initial spherical-grain morphology was replaced by angular grains with a few dispersed spherical grains (coarsened Ni grains by EDS analysis). This micrograph demonstrates that the method of *in situ* reduction could be utilized to form a cermet anode structure consisting of dispersed Ni-metal particulates over a W-based support structure, but the high temperature and fuel conditions lead to unwanted microstructural evolution. This coarsening of the granular structure was expected, especially for a microstructure that initially contains Ni nano-particulates. Typical microstructural evolution has not limited the application of traditional Ni/YSZ cermets containing micron-size precursor powders, but researchers have indicated that sintering/coarsening mechanisms can be detrimental for nanomaterial-containing electrodes [43,44]. The driving forces for sintering and coarsening for the Ni nanomaterials are exceedingly high, which results in severing of the

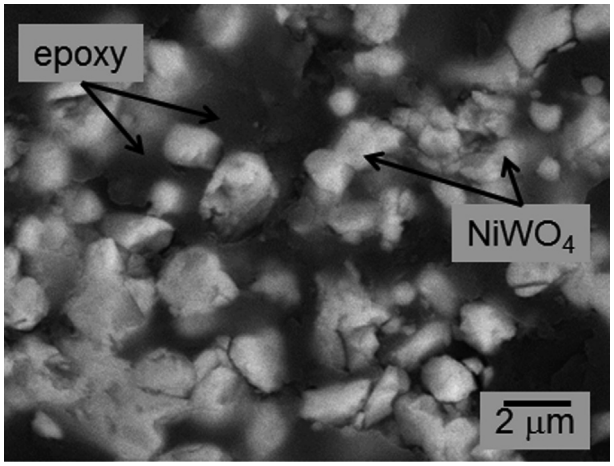


**Fig. 2.** Back-scattered SEM micrograph of the clean un-reduced $NiWO_4$ anode.

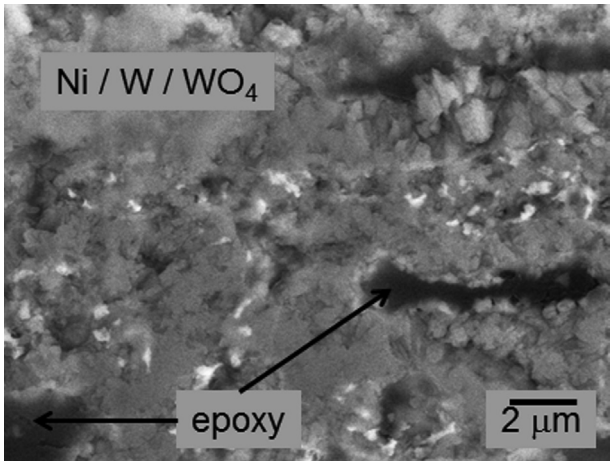


**Fig. 3.** Back-scattered SEM micrograph of the Ni/$WO_x$ anode after 48 h testing under a constant current load at 800 °C in clean $H_2$.

percolated network and a large reduction of the desired triple-phase boundary area.

### 3.2. X-ray photoelectron analysis of $NiWO_4$ anode after SOFC testing

The XPS depth profiling of the SOFC is shown in Fig. 4, where the 0 μm marker represents the outside surface of the anode, and the entire anode thickness was roughly 15 μm (thus, the electrolyte interface is at ~15 μm). The figure shows that the tungsten concentration throughout the cell does not change considerably; however, the nickel concentration decreases rapidly toward the interface. Fig. 5 shows the detailed spectra from the data presented above for the Ni $2p_{3/2}$ and $2p_{1/2}$ doublets, which are positioned at 852.8 (and 870.1) eV, 852.8 (and 870.1) eV and 852.7 (and 870.0) eV for 1.0, 7.5 and 15.0 μm depths from the surface, respectively. All these binding energy values agree well with chemical state values for pure Ni at 852.7 ± 0.1 and 869.9 ± 0.1 eV [45]. Therefore, it is fair to claim that the reduction process resulted in precipitation of pure Ni metal, and the state of the Ni was preserved after the SOFC testing with no atmospheric $O_2$ leaking into the anode chamber during cooling.

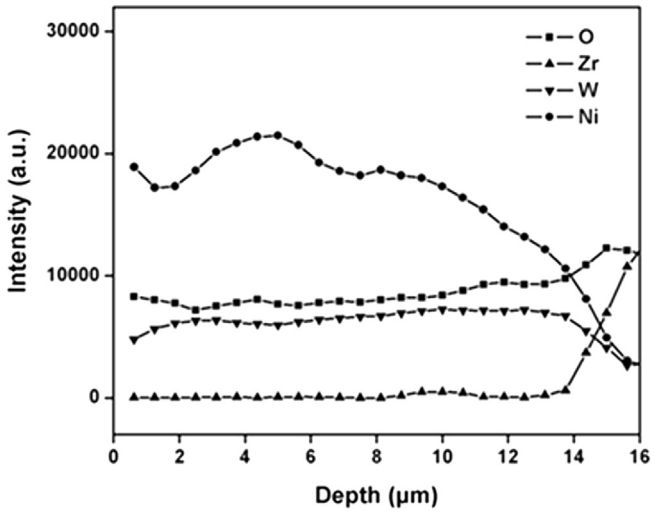


**Fig. 4.** XPS depth profiling of the $NiWO_4$/GDC anode tested on an electrolyte-supported cell at 800 °C in clean $H_2$.

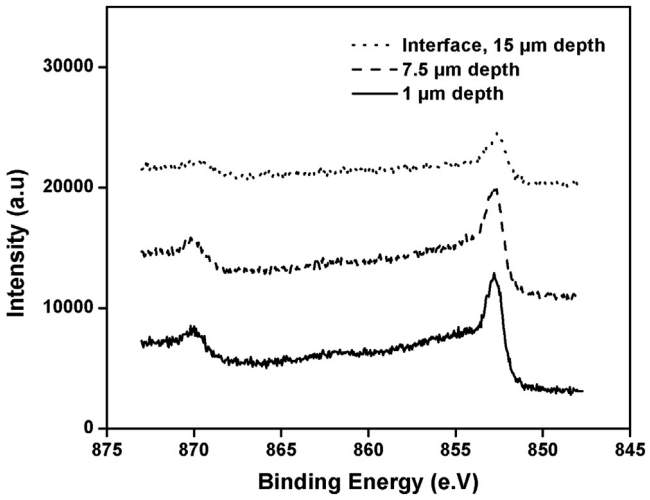


**Fig. 5.** Ni 2p detailed XPS spectra at three different depths of the $NiWO_4$/GDC anode tested on an electrolyte-supported cell at 800 °C in clean $H_2$.

Fig. 6 displays the detailed scan of W 4f peaks at the same depth as was previously described for the Ni in Fig. 5. Both the W $4f_{7/2}$ and $4f_{5/2}$ peaks were used to calculate the ratio of the different chemical states of W by integrating the area under the fitted peaks. In each case, the W metallic phase 4f peaks were observed at 31.6 and 33.7 eV with 2.1 eV spin-orbital splitting. The $WO_3$ 4f peak positions were determined to be at 35.6 and 37.7 eV for all three depths. These measured binding energies are in a good accordance with values found in the literature [45,46]. Table 1 includes the calculated fractions of the different oxidation states of tungsten de-convoluted from the W 4f spectrum at the three different depths. Fig. 6a shows that the top region (surface) of the cell consisted of a mixture of $WO_3$, $WO_2$ and W, as expected. However, it is noteworthy to indicate that broadening of $WO_2$ peaks indicates formation of various oxidation states. The $WO_2$ concentration did not show significant changes through the thickness of the coating. Approximately 14.50% of the tungsten was in the chemical state of $WO_2$ at the 1 μm depth, and slightly decreased to 11.8% and 11.31% at the middle zone (7.5 μm depth) and electrolyte interface, respectively. The peak positions of the $WO_2$ 4f were 33.6 and 35.7 eV which are also in a good agreement with the corresponding literature values [46]. $W^{+5}$ was first determined significantly at the 7.5 μm depth with value of 34.4 eV and 36.5 eV, and at the interface with 34.3 eV and 36.4 eV binding energies. This slight difference can be attributed to different types of sub-oxidation states which resulted in the broadening of the corresponding peaks. However, the values found for $W^{+5}$ are in good agreement with the literature value of 34.5 eV [46]. Fig. 6b clearly shows that at the middle of the cell thickness there was a considerable amount of the $W^{+5}$ (4.50%) and this chemical state increased to 9.83% at the interface. The composition of tungsten at the anode/electrolyte interface was comprised of 60% of different tungsten oxides, mainly $WO_3$, and 40% tungsten metal. It is known that argon ion etching during XPS depth profiling has a considerable effect on the reduction of the tungsten oxide compositions [47,48]. Therefore, it is believed that the near-electrolyte interface has potentially a lower amount of W metal than that measured in this study. Another important aspect of the study was that the amount of tungsten oxide decreased with decreasing distance to the electrolyte interface. This is opposite to the expected trend. The higher localized oxygen and steam partial pressure near the electrolyte interface should have stabilized the oxide form. The reason for the obtained trend is not evident at this time. Again, the SOFC anode compartment was cooled in flowing hydrogen and the presence of

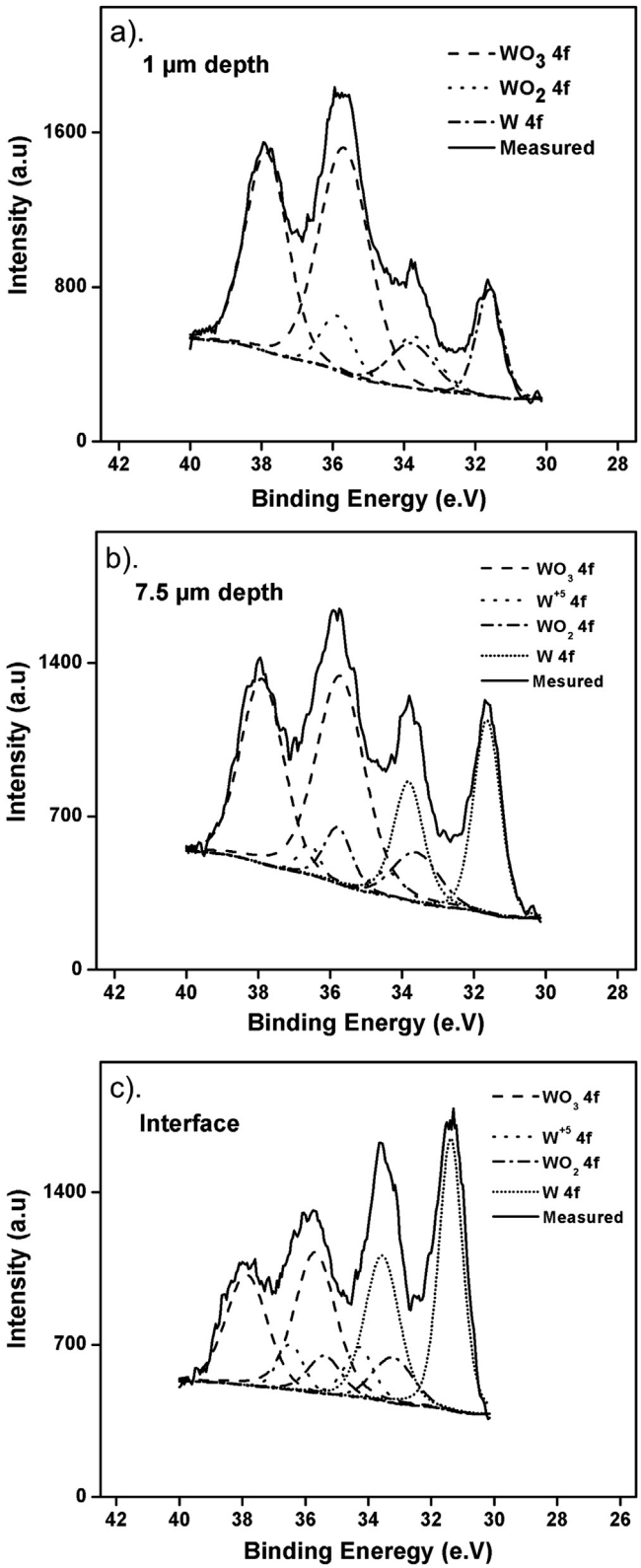


**Fig. 6.** Fitted W4f core spectra at three different depths: a) 1 μm, b) 7.5 μm, and c) 15 μm (electrolyte interface).

only Ni metal identified in the XPS spectrum reinforces this atmospheric state. In addition, any post-oxidation processes during ambient storage also could not contribute to the higher oxidation content at the outer surface (and lower W metal content), since the oxidation kinetics of tungsten metal is known to be quite low below 300 °C [49,50]. Therefore, the confidence in the measured tungsten metal and oxide content across the anode thickness is high, and thus, this distribution can be attributed to the anode functionality within the $H_2$ fuel.

**Table 1**
Concentration of the $WO_3$, $WO_2$ and W at the three different anode depths.

| Depth from surface (μm) | W | $WO_2$ | $W^{+5}$ | $WO_3$ |
|---|---|---|---|---|
| 1 | 17.19% | 14.50% | – | 68.31% |
| 7.5 | 27.48% | 11.80% | 4.5% | 56.02% |
| 15 (interface) | 40.84% | 11.31% | 9.83% | 38.01% |

### 3.3. Voltage–current–power testing of $NiWO_4$ anode with $PH_3$ impurity

After the baseline testing and compositional analysis, extended loading testing of the $NiWO_4$/GDC anode was completed by holding the pre-reduced sample at a constant load of 0.15 A $cm^{-2}$ for approximately 20 h at 800 °C to confirm stability of the anode in wet $H_2$ (Fig. 7). For the first 2 h of the run, there was a 7.7% increase in power density; after this point, there was a scattered response with a slow average decay in the performance for the next ~18 h. Linear regression was used to fit the decay after the maximum power was achieved. The average loss over this period as defined by the linear fit for the scattered data was ~2.3% until the phosphine was turned on within the system (or ~0.6% gain in power from the initial loading). The slight fluctuation in the cell voltage during the initial 20 h run was attributed to the drastic change in temperature and humidity of the ambient overnight, but changes in the microstructure due to coarsening and sintering mechanisms may also have an influence on the slow degradation.

After 24 h, 10 ppm $PH_3$ was added into the $H_2$ fuel stream. Within a matter of minutes, the cell voltage began to decrease. During the first 5 h of impurity testing, the rate of degradation was ~0.006 V $h^{-1}$. Beyond that time period, the degradation rate increased to ~0.015 V $h^{-1}$. The cell voltage decreased at this rate until it reached 0.05 V, after which the $PH_3$ impurity was cutoff and the cell was cooled.

The EIS spectrum of the cell in clean $H_2$ showed an ohmic resistance of ~1 Ω $cm^2$, which is rather high since only ~0.35–

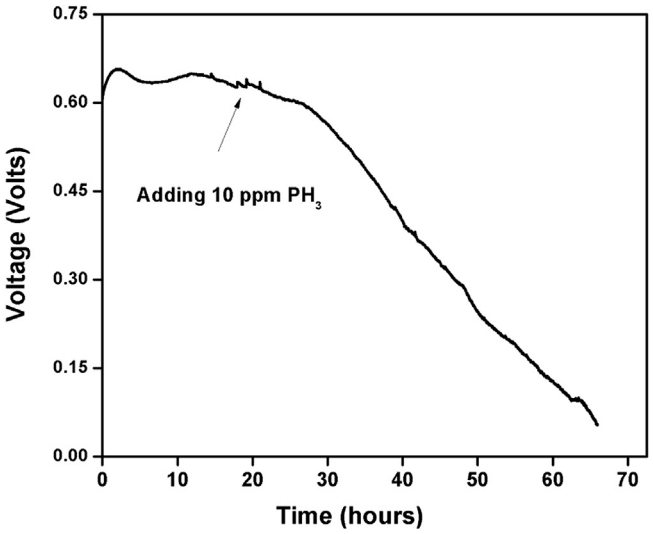


**Fig. 7.** Cell voltage as function of time for an electrolyte-supported SOFC button cell with a $NiWO_4$/GDC anode tested at a current density of 0.15 A $cm^{-2}$ at 800 °C.

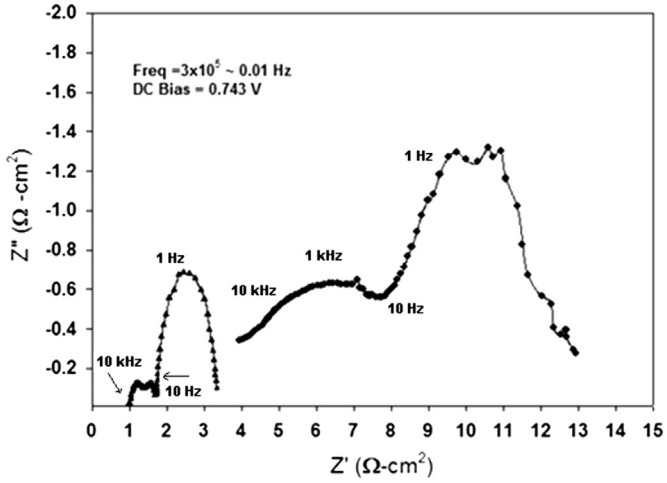


**Fig. 8.** EIS data of an entire SOFC button cell with a $NiWO_4$/GDC anode before and after 10 ppm $PH_3$ impurity addition within the humidified $H_2$ fuel.

0.4 Ω $cm^2$ should be aligned with the thicker YSZ electrolyte (~120 μm and conductivity of 0.035 S $cm^{-1}$ at 800 °C). The additional ohmic resistance may be attributed to limitations in the current collection or potential reaction between the electrolyte and $WO_x$/W phases. The initial total polarization resistance was found to be 2.4 Ω $cm^2$. This elevated resistance in comparison to the traditional Ni/YSZ electrolyte-supported cell was attributed to both diffusion limitations and the alteration in the TPB morphology due to microstructural changes during reduction. After running the cell for 45 h in 10 ppm $PH_3$, the total cell resistance increased to over 10 Ω $cm^2$. The EIS data for the cell in clean $H_2$ and $H_2$ + 10 ppm $PH_3$ under 300 mV DC bias can be seen in Fig. 8.

Cross-sectional SEM images taken from the cell measured using the above-discussed protocol showed that the relatively uniform anode microstructure in the clean, reduced environment was replaced with numerous coarse particulates after poisoning. Previous research has shown that this concentration of $PH_3$ in the fuel stream leads to different attack mechanisms for the traditional Ni/YSZ cell. Xu et al. [51] found that for an anode-supported Ni/YSZ cell operating in syngas with 10 ppm $PH_3$, Ni migration to the anode surface in the form of liquid Ni–P phases was the predominant feature of the microstructure, and that $Ni_2P_5$ was the most probable resultant phase based on post-test characterization and thermodynamic analysis. X-ray photoelectron spectroscopy (XPS) of the anode surface contained strong peaks for the phosphorus 2p core level as seen in Fig. 9. Furthermore, the energy dispersive spectroscopy (EDS) scan of the anode–electrolyte interface also indicated a strong P peak. The phosphorus 2p peak positioned at about 133.5 eV suggested that a phosphate presence exists on the electrode surface. However, the lack of a peak in the 126–128 eV range indicated that Ni–P and W–P chemisorption did not occur for this fuel condition. The $PH_3$ did however drastically reduce the cell performance, and thus, it is reasonable to state that for the 10 ppm concentration of $PH_3$, the $NiWO_4$-based anode experiences a similar degradation mechanism to the Ni–YSZ cermet.

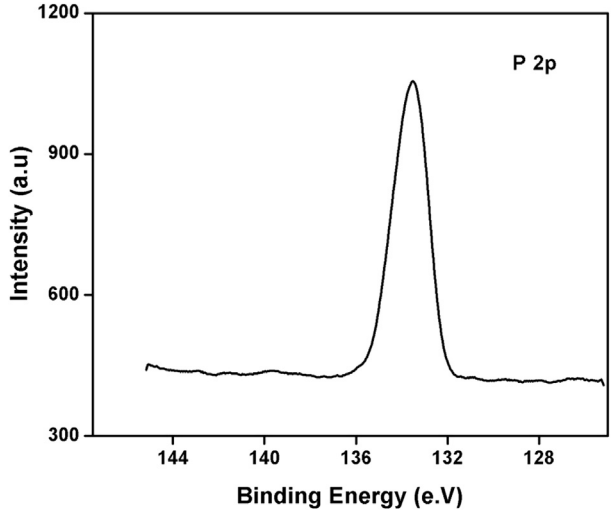


**Fig. 9.** XPS spectra for the P 2p peak measured from the surface of the loaded $NiWO_4$/GDC anode after 10 ppm $PH_3$ impurity addition.

## 4. Conclusions

The work demonstrated the method of *in situ* reduction of a ternary oxide composition to form a cermet composition that may be utilized as a SOFC anode. In this work, the $NiWO_4$ composition was chosen since the reduced oxide would result in a mixture of Ni metal and a MIEC oxide, which is the typical cermet combination required for the electrochemical reaction within SOFC anodes. The proposed $NiWO_4$ composition successfully demonstrated adequate performance for an un-optimized microstructure on a rather thick YSZ membrane utilizing LSM as the cathode. Additionally, the anode sintering temperatures were compatible with conventional SOFC cathodes making co-sintering of the anode with high-performance ferrite and cobaltite cathodes possible. Further testing of the reduced $NiWO_4$ anode indicated that there may be a deficiency in ionic carrier paths and reaction sites within the anode structure. The performance of the formed cermet was improved with the incorporation of both YSZ and GDC into the anode matrix. GDC in particular increased the power output of a single cell by almost 58%. Although the $NiWO_4$ composition did not result in the optimal performance, the technique of utilizing an *in situ* reduction process of a ternary oxide (containing base or precious metals) showed great promise. This work demonstration provides a path to research on further ternary compositions that result in cermets containing redox stable MIECs, unlike the current cermet composition containing $WO_3$. XPS analysis did confirm that significant levels of $WO_x$ were present in the oxygen depleted anodic atmosphere. This work also verified that a Ni/$WO_x$/GDC anode demonstrated similar problems to the Ni/YSZ cermets in regards to $PH_3$ tolerance; specifically, a coarsened microstructure and surface phosphate/nickel-phosphide presence that caused cell failure within 45 h.

## Acknowledgments

The authors would like to acknowledge the financial support from the US DOE Office of Basic Energy Sciences, NETL (National Energy Technology Laboratory), WV State EPSCoR Office, and West Virginia University under grant number DE-FG02-06ER46299. Ms. Adrienne MacLeod, Joshua Mullenax, Dr. Hui Zhang, Dr.Wei Ding and WVU Shared Research Facilities are thanked for assistance with the SEM, EDS, and XPS characterization. The authors would also like to thank Rege Perich and Marc Palmisiano at ANH Refractories Technical Center (West Mifflin, PA) for their assistance with isostatic pressing of samples.

## References

[1] S.-D. Kim, H. Moon, S.-H. Hyun, J. Moon, J. Kim, H.-W. Lee, Solid State Ion. 177 (2006) 931–938.
[2] M. Mogensen, S. Skaarup, Solid State Ion. 86–88 (1996) 1151–1160.

[3] F.N. Cayan, M. Zhi, S.R. Pakalapati, I. Celik, N. Wu, R. Gemmen, J. Power Sources 185 (2008) 595–602.
[4] E.V. Tsipis, V.V. Kharton, J. Solid State Electrochem. 12 (2008) 1367–1391.
[5] E.V. Tsipis, V.V. Kharton, J. Solid State Electrochem. 15 (2011) 1007–1040.
[6] G.J. Offer, J. Mermelstein, E. Brightman, N.P. Brandon, J. Am. Ceram. Soc. 92 (2009) 763–780.
[7] M.R. Pillai, I. Kim, D.M. Bierschenk, S.A. Barnett, J. Power Sources 185 (2008) 1086–1093.
[8] Q. Ma, F. Tietz, A. Leonide, E. Ivers-Tiffée, Electrochem. Commun. 12 (2010) 1326–1328.
[9] H. Ding, J. Ge, X. Xue, Solid-State Lett. 15 (2012) 86–89.
[10] X.J. Chen, Q.L. Liu, S.H. Chan, N.P. Brandon, K.A. Khor, Electrochem. Commun. 9 (2007) 767–772.
[11] P. Vozdecky, A. Roosen, Q. Ma, F. Tietz, H. Buchkremer, J. Mater. Sci. 46 (2011) 3493–3499.
[12] J.B. Goodenough, Y. Huang, J. Power Sources 173 (2007) 1–10.
[13] P. Gansor, C. Xu, K. Sabolsky, J.W. Zondlo, E.M. Sabolsky, J. Power Sources 198 (2012) 7–13.
[14] S. Wang, Y. He, J. Zo, Y. Wang, H. Huang, J. Alloys Compd. 482 (2009) 61–66.
[15] C. Yates, J. Winnick, J. Electrochem. Soc. 146 (1999) 2841–2844.
[16] A. Torabi, T.H. Etsell, N. Semagina, P. Sarkar, Electrochim. Acta 67 (2012) 172–180.
[17] A. Torabi, T.H. Etsell, J. Electrochem. Soc. 159 (2012) B714–B722.
[18] B. Solsona, J.M. López Nieto, P. Concepción, A. Dejoz, F. Ivars, M.I. Vázquez, J. Catal. 280 (2011) 28–39.
[19] E. Antolini, E.R. Gonzalez, Appl. Catal. B Environ. 96 (2010) 245–266.
[20] B. Fruhberger, M. Grunze, D.J. Dwyer, Sens. Actuators B Chem. (1996) 167–174.
[21] A. Stankova, X. Vilanova, J. Calderer, E. Llobet, P. Ivanov, I. Gracia, C. Cane, X. Correig, Sens. Actuators 102 (2004) 219–225.
[22] P. Atanasova, T. Tabakova, C. Vladov, T. Halachev, A. Lopez Agudo, Appl. Catal. A Gen. 161 (1997) 105–119.
[23] A.M. Hussain, B.R. Sudireddy, J.V.T. Høgh, N. Bonanos, Fuel Cells 12 (2012) 530–536.
[24] S. Sridhar, S.C. Du, S. Seetharaman, Metall. Mater. Trans. B 25 (1994) 391–396.
[25] J.A. Bustnes, D. Sichen, S. Seetharaman, Scand. J. Metall. 29 (2000) 151–155.
[26] J.A. Bustnes, Metall. Mater. Trans. B 29 (1998) 1136–1139.
[27] G. Orsini, V. Tricoli, J. Mater. Chem. 21 (2011) 14530–14542.
[28] J. Guerin, K. Aguir, M. Bendahan, Sens. Actuators B Chem. 119 (2006) 327–334.
[29] A. Labidi, C. Jacolin, M. Bendahan, A. Abdelghani, J. Guerin, K. Aguir, M. Maaref, Sens. Actuators B Chem. 106 (2005) 713–718.
[30] M.G. Hutchins, O. Abu-Alkhair, M.M. El-Nahass, K. Abdel-Hady, J. Phys. Condens. Matter 18 (2006) 9987–9997.
[31] J. Alvarez, G. Valderrama, E. Pietri, M.J. Perez-Zurita, C.U. de Navarro, E.F. Sousa-Aguiar, M.R. Goldwasser, Top. Catal. 54 (2011) 170–178.
[32] M.R. Goldwasser, M.E. Rivas, M.L. Lugo, E. Pietri, J. Perez-Zurita, M.L. Cubeiro, A. Griboval-Constant, G. Leclercq, Catal. Today 107–108 (2005) 106–113.
[33] M.R. Goldwasser, M.E. Rivas, E. Pietri, M.J. Pérez-Zurita, M.L. Cubeiro, L. Gingembre, L. Leclercq, G. Leclercq, Appl. Catal. A Gen. 255 (2003) 45–57.
[34] B. Pillay, M.R. Mathebula, H.B. Friedrich, Catal. Lett. 141 (2011) 1297–1304.
[35] B. Pillay, M.R. Mathebula, H.B. Friedrich, Appl. Catal. A Gen. 361 (2009) 57–64.
[36] O.A. Knayazheva, O.N. Baklanova, A.V. Lavrenov, V.A. Drozdov, N.N. Leont'eva, M.V. Trenikhin, A.B. Arbuzov, V.A. Likholobov, Kinet. Catal. 52 (2011) 886–895.
[37] L. Wang, W. Chu, C. Jiang, Y. Liu, J. Wen, Z. Xie, J. Nat. Gas Chem. 21 (2012) 43–48.
[38] R.S. Gemmen, J. Trembly, J. Power Sources 161 (2006) 1084–1095.
[39] G. Krishnan, in: Proc. 9th Annual Solid State Energy Conversion Alliance Workshop, Pittsburgh, PA, USA, August 5–7, 2008.
[40] J.P. Trembly, R.S. Gemmen, D.J. Bayless, in: Proc. 5th International Fuel Cell Science, Engineering and Technology Conference, New York, NY, 2007.
[41] M.J. Zhi, X.Q. Chen, H. Finklea, I. Celik, N.Q. Wu, J. Power Sources 183 (2008) 485–490.
[42] O.A. Marina, C.A. Coyle, E.C. Thomsen, D.J. Edwards, G.W. Coffey, L.R. Pederson, Solid State Ion. 181 (2010) 430–440.
[43] H.-Y. Chen, H.-C. Yu, J.S. Cronin, J.R. Wilson, S.A. Barnett, K. Thornton, J. Power Sources 196 (2011) 1333–1337.
[44] T. Klemensø, K. Thydén, M. Chen, H.-J. Wang, J. Power Sources 195 (2010) 7295–7301.
[45] J.F. Moulder, W.F. Stickle, P.E. Sobol, K.D. Bomben, Handbook of X-ray Photoelectron Spectroscopy, ULVAC-PHI. Inc., Chigasaki, Japan, 1995. pp. 84–85 and 172–173.
[46] S. Jeon, K. Yong, J. Mater. Res. 23 (2008) 1320–1326.
[47] M. Katoh, Y. Takeda, Jpn. J. Appl. Phys. 43 (2004) 7292–7295.
[48] F.Y. Xie, L. Gong, X. Liu, Y.T. Tao, W.H. Zhang, S.H. Chen, H. Meng, J. Chen, J. Electron. Spectrosc. 185 (2012) 112–118.
[49] A. Warren, A. Nylund, I. Olefjord, Int. J. Refract. Met. Hard Mater. 14 (1996) 345–353.
[50] R. Sohal, C. Walczyk, P. Zaumseil, D. Wolansky, A. Fox, B. Tillack, H. Müssig, T. Schroeder, Thin Solid Films 517 (2009) 4534–4539.
[51] C. Xu, J.W. Zondlo, H. Finklea, O. Demircan, M. Gong, X. Liu, J. Power Sources 193 (2009) 739–746.